

Material-Intrinsic NIR-Fluorescence Enables Image-Guided Surgery for Ceramic Fracture Removal

Robert Nifßler,* Elena Totter, Sebastian G. Walter,* Justus T. Metternich, Oscar Cipolato, Dimitri Nowack, Alexander Gogos, and Inge K. Herrmann*

Hip arthroplasty effectively treats advanced osteoarthritis and is therefore entitled as “operation of the 20th century.” With demographic shifts, the USA alone is projected to perform up to 850 000 arthroplasties annually by 2030. Many implants now feature a ceramic head, valued for strength and wear resistance. Nonetheless, a fraction, up to 0.03% may fracture during their lifespan, demanding complex removal procedures. To address this, a radiation-free, fluorescence-based image-guided surgical technique is presented. The method uses the inherent fluorescence of ceramic implant materials, demonstrated through chemical and optical analysis of prevalent implant types. Specifically, BioloX delta implants exhibited strong fluorescence around 700 nm with a 74% photoluminescence quantum yield. Emission tails are identified extending into the near-infrared (NIR-I) biological transparency range, forming a vital prerequisite for the label-free visualization of fragments. This ruby-like fluorescence could be attributed to Cr within the zirconia-toughened alumina matrix, enabling the detection of even deep-seated millimeter-sized fragments via camera-assisted techniques. Additionally, fluorescence microscopy allowed detection of μm -sized ceramic particles, enabling debris visualization in synovial fluid as well as histological samples. This label-free optical imaging approach employs readily accessible equipment and can seamlessly transition to clinical settings without significant regulatory barriers, thereby enhancing the safety, efficiency, and minimally invasive nature of fractured ceramic implant removal procedures.

1. Introduction

Total hip arthroplasty (THA) is a safe and highly standardized treatment procedure for symptomatic and advanced osteoarthritis of the hip joint and has, therefore, been entitled an “operation of the 20th century.”^[1] Worldwide, more than a million THAs are performed each year.^[2–4] Due to demographic changes within these regions, the number of THAs performed is forecasted to grow continuously within the upcoming decades, reaching annually 635 000–850 000 THA by 2030 in the USA alone and several millions on a global scale.^[5,6] Hip implants are installed either with a ceramic head on a polyethylene articulation (highly crosslinked UHMWPE, highly crosslinked PE), a metal-on-polyethylene, or a ceramic-on-ceramic (CoC) bearing. Ceramics used for implant manufacturing of femoral heads or acetabular cup liners are based on pure aluminum oxide, zirconia-toughened alumina (ZTA), alumina-toughened zirconia (ATZ), or yttrium-stabilized zirconia (Y-ZrO₂).^[7] Modern third- and fourth-generation ceramics comprise an alumina

R. Nifßler, E. Totter, O. Cipolato, A. Gogos, I. K. Herrmann
Nanoparticle Systems Engineering Laboratory
Institute of Energy and Process Engineering (IEPE)
Department of Mechanical and Process Engineering (D-MAVT)
ETH Zurich

Sonneggstrasse 3, Zurich 8092, Switzerland
E-mail: rnissler@ethz.ch; ingeh@ethz.ch

R. Nifßler, O. Cipolato, A. Gogos, I. K. Herrmann
Particles-Biology Interactions
Department of Materials Meet Life
Swiss Federal Laboratories for Materials Science and Technology (Empa)
Lerchenfeldstrasse 5, St. Gallen 9014, Switzerland

R. Nifßler, O. Cipolato, I. K. Herrmann
The Ingenuity Lab
University Hospital Balgrist
University of Zurich
Forchstrasse 340, Zurich 8008, Switzerland

S. G. Walter
Department of Orthopedics
Traumatology and Reconstructive Surgery
University Hospital Cologne
Joseph-Stelzmann-Str. 24, 50931 Cologne, Germany
E-mail: sebastian.walter@uk-koeln.de

J. T. Metternich
Physical Chemistry
Ruhr-University Bochum
Universitätsstr. 150, 44801 Bochum, Germany

J. T. Metternich
Fraunhofer Institute for Microelectronic Circuits and Systems (IMS)
Finkenstr. 61, 47057 Duisburg, Germany

 The ORCID identification number(s) for the author(s) of this article can be found under <https://doi.org/10.1002/adhm.202302950>

© 2024 The Authors. Advanced Healthcare Materials published by Wiley-VCH GmbH. This is an open access article under the terms of the [Creative Commons Attribution-NonCommercial](https://creativecommons.org/licenses/by-nc/4.0/) License, which permits use, distribution and reproduction in any medium, provided the original work is properly cited and is not used for commercial purposes.

DOI: 10.1002/adhm.202302950

base with fractions of zirconia, chromium, strontium, and other minor constituents. State-of-the-art ceramic implants are biologically inert, corrosion resistant, have good lubrication properties, and are less brittle compared to previous generations.^[8] CoC articulation is increasingly used because of its lower wear rates ($5 \mu\text{m year}^{-1}$) compared to ceramic-on-polyethylene (CoP) articulation ($50 \mu\text{m year}^{-1}$) over 20 years.^[9] Although wear rates are low and the risk of aseptic loosening is reduced in CoC bearings, this complication cannot be fully excluded.^[10] Analogous to the particle diseases known for polyethylene and metal bearings, agglomerates of ceramic abrasion particles have been observed in cells in proximity of the implant, along with regions affected by necrosis or necrobiosis.^[11] However, there are typically fewer foreign body giant cells found for ceramic implants compared with metal-on-polyethylene bearings.^[12] In addition to wear and tear, up to 0.03% of implanted ceramics break within their lifetime.^[13,14] In most cases, breakage occurs within the first 48 months after implantation, and fragment sizes ranging from several micrometers to centimeters cause severe problems.^[14,15] Typical wear particles generated during wear and tear can be detected within the synovial fluid; however, they are typically in the sub-micron range and thus difficult to detect and retrieve.^[16] Both, aseptic loosening and ceramic breakage can create major orthopedic problems requiring revision surgery to reconstruct lost bone stock and/or remove ceramic fractures.^[13] This procedure can be challenging and may require extensive synovectomy and capsulectomy as the complete removal, especially of small fragments, is difficult due to the poor visualization capabilities in soft tissue.^[17,18] While X-ray imaging is applicable in principle, it is based on ionizing radiation and limited in sensitivity/resolution, hence not allowing straightforward intraoperative detection of small fragments. The state-of-the-art techniques, used to detect and remove ceramic debris, are mainly based on the technical skills of the surgeon, and fragments are identified through palpation and haptic feedback.

Interestingly, certain types of ceramics are known to have (intrinsic) fluorescent properties. In a pure Al_2O_3 single crystal, oxygen atoms are arranged in a hexagonal close-packed structure with aluminum atoms occupying the octahedral gaps such that each aluminum atom is surrounded by six oxygen atoms. This creates a distorted octahedron with the space group $R3c$. In a perfect crystal with no impurities or defects, all electrons of the Al^{3+} cations within the alumina matrix are paired with the oxygen atoms in such a way that the material is nonfluorescent.^[19,20] Such a perfect crystal, however, cannot be found in nature and is difficult to produce. In most cases, alumina contains defects and trace elements, which may give rise to fluorescent properties. For example, $\alpha\text{-Al}_2\text{O}_3$ has a hexagonal crystal structure and typically contains traces of Cr^{3+} cations, which substitute the (slightly smaller) Al^{3+} cations.^[21,22] These natural impurities are typically confined to a concentration range of <60 ppm. Interestingly, the electrons of the Cr atoms can be excited using specific wavelengths of electromagnetic radiation and can relax back to

their ground state upon emitting photons, a phenomenon also known to occur in ruby, the naturally occurring Cr-doped variation of corundum.^[23–25] Hereby, electrons in the ground state ($^4\text{A}_{2g}$) can be excited using either blue or yellow–green light to higher energy states ($^4\text{T}_{1g}$ and $^4\text{T}_{2g}$) called the U-band or Y-band, respectively.^[26] From these two bands, the electrons relax back to the ^2E energy state without emitting photons. This energy state splits into two states due to anisotropy in the crystal structure (spin–orbit interactions), from which the electrons relax back to the ground state $^4\text{A}_{2g}$.^[23] These two relaxations result in the so-called R fluorescence lines: the R1 line at 692.8 nm and the R2 line at 694.2 nm, respectively, with a fluorescence lifetime of few milliseconds.^[24,26–28] Fluorescence behavior is not exclusive to $\alpha\text{-Al}_2\text{O}_3$, as it has been observed for various Al_2O_3 phases (γ , χ , θ , δ , α) with varying concentrations of Fe and Cr impurities.^[29,30] When analyzing the powders with higher Cr^{3+} concentrations (Cr-to-Al ratios), intense fluorescence lines at 692 and 694 nm were observed.^[31] However, these Cr^{3+} attributed emission lines were also observed in a Fe-doped sample, where the Cr impurities were found to be only 0.02 wt%. This suggests that even trace amounts of Cr^{3+} dopants are potentially sufficient to induce detectable fluorescence of these two R lines.^[32] Despite using highly pure aluminum oxide powder, fluorescence was found because of different uncontrolled trace impurities. A broad band at 750 nm in a $\delta\text{-Al}_2\text{O}_3$ phase powder was ascribed to Fe^{3+} ions, while a narrow band at 667 nm in the $\alpha\text{-Al}_2\text{O}_3$ phase was attributed to Mn^{4+} ions. The prominent R lines resulting from Cr^{3+} impurities were observed in all samples of different phases. Moreover, doping $\alpha\text{-Al}_2\text{O}_3$ with Mn^{4+} ions was shown to induce a bright luminescent feature at 675 nm, especially in combination with other co-dopants, such as Mg^{2+} , while $\text{Ti}^{3+}/\text{Ti}^{4+}$ doping leads to a fluorescence emission in the range of 420 and 750 nm.^[33–36] Interestingly, commercial ceramic implants also contain various amounts of trace contaminations, which may give rise to fluorescent properties. Such aforementioned fluorescence properties could open new routes for ionizing radiation-free ceramic material detection since imaging in the near-infrared range (NIR, 700–1700 nm) offers high tissue penetration by light in the so-called “biological transparency window.”^[37] This includes reduced light absorption from water and tissue, decreased photon scattering, and a strongly diminished autofluorescence background. The NIR range can generally be subdivided into the NIR-I (700–900 nm) and the NIR-II (1000–1700 nm) ranges, and a variety of prominent materials have been exploited as imaging contrast agents in these two biological windows.^[38] Such materials emitting in the NIR include organic structures, including dyes such as indocyanine green^[37] or BODIPY,^[39] as well as inorganic structures, including quantum dots,^[40] single-walled carbon nanotube,^[41,42] 2D-copper silicates^[43] or rare-earth (e.g., lanthanide) doped nanoparticles.^[44]

In this study, we sought to harness the so far unexploited NIR-fluorescence properties of aluminum oxide implant materials (such as ZTA used in commercial implant ceramics) for the intraoperative localization of ceramic fragments in periprosthetic tissue, as well as the detection of wear particles in synovial fluid in the context of hip arthroplasties. For this, commonly used ceramic implants were chemically and optically characterized, providing insights into the mechanisms responsible for the fluorescence emission in the NIR of existing commercial hip

D. Nowack
Deutsches Zentrum für Orthopädie
Department of Orthopedics and Trauma Surgery
Friedrich Schiller University Jena
Eisenberg, 07743 Jena, Germany

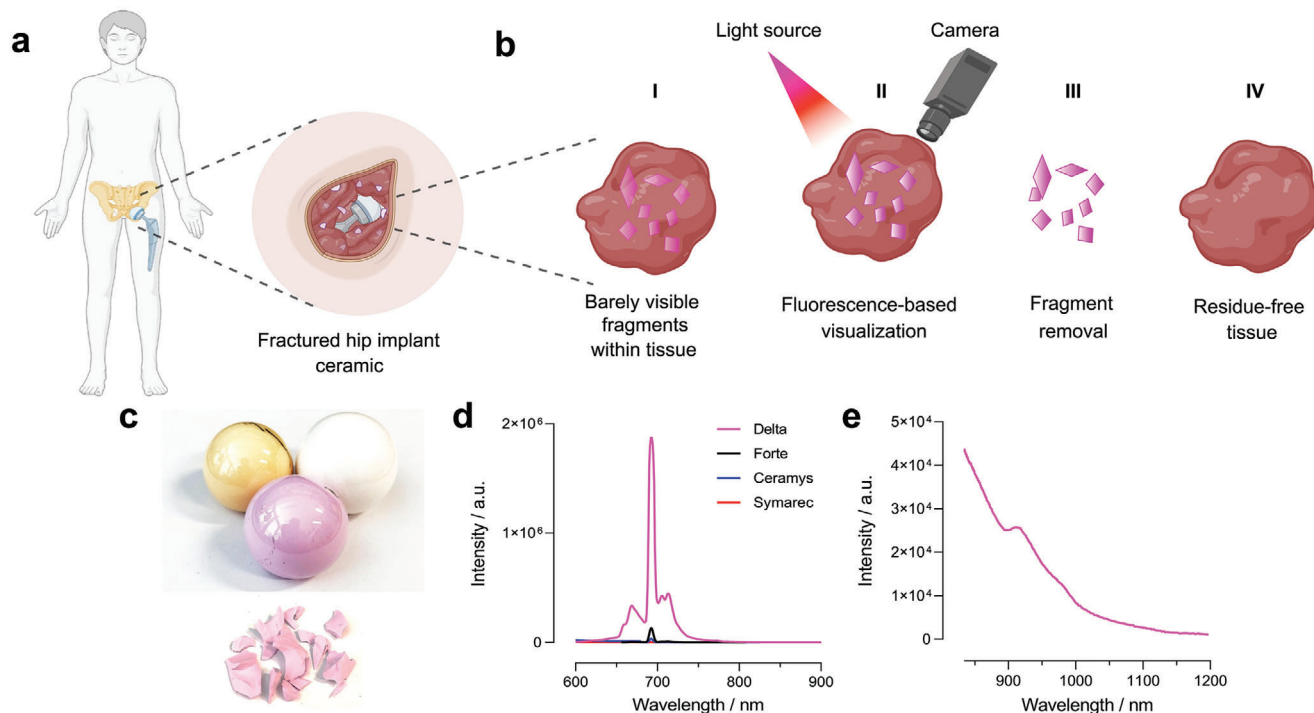


Figure 1. Schematic of NIR-image-guided surgery for the removal of fractured hip implant ceramics. a) Hip arthroplasty, usually implanting ceramic heads, is a highly common surgery; however, up to 0.03% of implants will fracture in their lifetime, causing severe damage and the need for urgent intervention. b) Exemplary workflow of the NIR-fluorescence-based fracture removal. Fragments of ceramic implants remain within the tissue (I), which makes localization and hence complete removal challenging. Camera-based visualization of the ceramic splinters (II) allows detection through tissue based on the ceramic-intrinsic fluorescent properties in the NIR-I biological transparency window. Hence, ceramic splinters and debris can be removed (III), resulting in ceramic debris-free tissue (IV). c) Image of commonly used ceramic implant femoral heads and splinters. Golden-Biolox forte; white-Ceramys; pink-Biolox delta. d) Fluorescence spectra of the four tested ceramic implant materials show the strongest emission around 700 nm for BioloX delta. Analysis was performed with a standard silicon-based detector optimized for the UV-vis region. e) A specialized InGaAs detector reveals a prominent NIR-fluorescence emission tail for BioloX delta.

implants. We then demonstrate the detection of Cr-containing implant fragments using a camera-based setup for intraoperative macroscopic fracture removal, as well as the microscopic detection of ceramic debris in synovial fluid-like samples. The presented strategy holds great promise as a label-free image-guided surgical approach for fragment removal, alongside a route to ceramic debris detection in synovial fluid samples and histological specimens in a straightforward manner. The exploitation of material-intrinsic optical properties for implant fragment and debris detection and recovery opens a readily translatable route to the design and safer use of ceramic implants in the future.

2. Results and Discussion

When it comes to ceramic failure after hip revision surgery, a fast and complete intervention is needed to prevent further damage to the joint tissue. While even the intraoperative removal of large ceramic splinters can be challenging, the localization of small fragments within the tissue is a major obstacle, resulting in a high rate of secondary implant failures (Figure 1a).^[45,46] Here, we introduce an NIR-fluorescence-guided approach, enabling the fast (real-time) detection of ceramic splinters by utilizing the intrinsic fluorescence properties of the most widely used hip cup ceram-

ics. The general principle is depicted in Figure 1, where illumination of the affected soft tissue with a light source and concurrent imaging with a camera enables visualization of otherwise invisible ceramic splinters. This straightforward localization of fragments allows for their complete removal and hence a ceramic residue-free joint tissue.

2.1. Physicochemical Characterization of Commercial Implant Ceramics

To investigate the feasibility of this approach for commercially important implants, several of the most commonly used ceramic implant femoral heads were investigated, namely, BioloX forte, BioloX delta (CeramTec), Ceramys, and Symarec (Mathys) (Figure 1c). While all of these clinically established ceramics exhibit a characteristic emission at 693 nm, in-depth analysis of their fluorescence properties revealed pronounced differences in the emission intensities and profiles (Figure 1d). BioloX delta exhibited the strongest and Ceramys the weakest emission intensity (Supporting Information Figure S1). Interestingly, for BioloX delta, a fluorescence feature at 720 nm in the NIR-I is detectable, even when using a standard, silicon-based detector. Such emission in the NIR becomes even more prominent, with

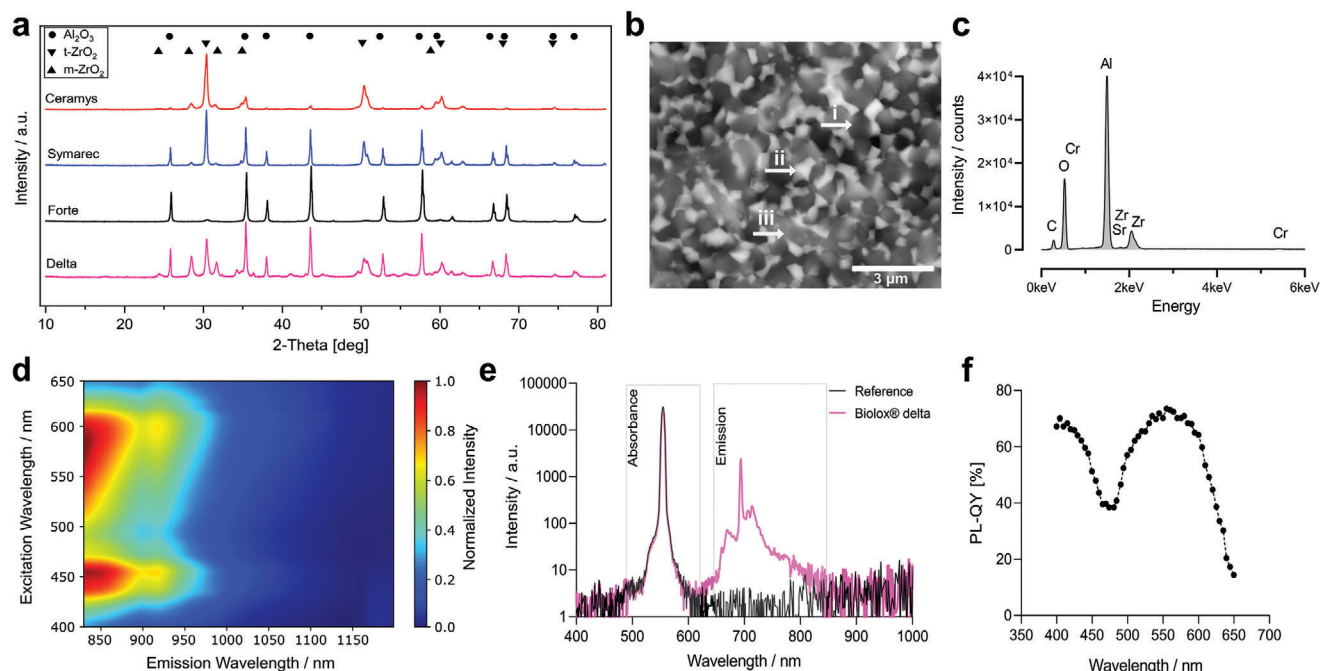


Figure 2. Ceramic implant material characterization: Composition and PL. a) XRD pattern of ZTA implant ceramics. b) SEM analysis of BioloX delta reveals largely sintered areas. The backscattered electron (BSE) image shows a clear mass contrast between i- Al_2O_3 , ii- ZrO_2 , and iii-SrO (see also Supporting Information Figure S2). c) EDX spectra of BioloX delta ceramics show the main elemental composition (carbon (C) introduced through sputtering during sample preparation). d) 2D NIR excitation–emission map of BioloX delta ceramic shows a strong emission tail in the NIR up to 1000 nm. e) Absolute quantum yield spectrum of BioloX delta. f) Excitation wavelengths dependent on absolute quantum yield for BioloX delta, with a maximum at 550 nm and 74% QY, integrated photon counts from 640 to 830 nm.

an InGaAs-detector optimized for this spectral region, revealing a large emission tail of BioloX delta until 1000 nm (Figure 1e). To understand these differences between different commercial implants more comprehensively, the chemical and mineral composition of the ceramic materials was analyzed in detail. The (ZTA) implant ceramic materials were processed in a ball mill yielding fine particles suitable for powder diffractometry (X-ray diffraction (XRD)). XRD analysis and subsequent Rietveld refinement revealed a mineral composition in line with the specification of the manufacturers (Supporting Information Table S1). All ceramics contained α - Al_2O_3 . ZrO_2 was detected in varying concentrations (0–80%) and as a mixture between the tetragonal (t) and monocline (m)- ZrO_2 crystal phases. Such differences likely result from the manufacturing process and the respective sintering temperatures during manufacturing.^[47] Further material characterization using scanning electron microscopy (SEM, Figure 2b) revealed sintered domains of Al_2O_3 , ZrO_2 , and SrO within BioloX delta (Supporting Information Figure S2). In addition, energy dispersive X-ray spectroscopy (EDX) indicated a Cr content of $\approx 0.3\%$ within the ZTA ceramic matrix of BioloX delta (Figure 2c), used by the manufacturer as an additive to improve the mechanical stability. Following compositional and phase analysis, we aimed to link the material properties to the photoluminescence (PL) characteristics to better understand the enhanced NIR emission observed for BioloX delta compared to the other implant materials. After acquiring a 2D NIR excitation–emission map, it becomes evident that BioloX delta can be most efficiently excited at wavelengths of 450 and 570 nm, resulting

in a strong NIR emission tail up to 1000 nm. It should be mentioned that the used optical setup, equipped with an InGaAs detector, allows for the detection of light with a wavelength of 820 nm (corresponding to the highest measured intensity) or higher as the NIR emission tail decreases. However, upon using a silicon-based detector that covers most of the emission tail, a static decay becomes apparent (Supporting Information Figures S3 and S4). To quantify the emission intensity, absolute quantum yield spectroscopy was applied. The BioloX delta sample absorbs a fraction of the excitation light, while the emitted photons are strongly visible in a region between 640 and 830 nm (Figure 2e). This results in a remarkably high maximum quantum yield of 74% at an excitation wavelength of 550 nm. The detected absolute PL quantum yield (PL-QY) of BioloX delta ZTA falls hereby in the same range as the one described for ruby (63–90%), the naturally occurring Cr-doped corundum (α - Al_2O_3).^[48–50] Variation in the excitation wavelength further allows assessment of the dependency of the quantum yield on the excitation light (Figure 2f). Such obtained information can later be used to select the most efficient excitation light source for the illumination of the ceramic splinters. Absolute quantum yield analysis of the other investigated ceramic implant materials yielded maximal quantum yields of 8% for BioloX forte, 1% for Symarec, and $<0.05\%$ for Ceramys.

The described fluorescent features of the ZTA ceramics align with previous reports, typically used to study boundary-induced strain on the ceramic surface.^[22,51,52] The main emission at 693 nm shows features similar to the naturally occurring ruby

(Al₂O₃ doped with Cr³⁺). This, together with obtained data, suggests that the overall emission of ZTA ceramics depends on the Al₂O₃ content and the potential Cr doping. This hypothesis is further supported by the observation that Ceramys ceramics, containing only 20% Al₂O₃, showed the lowest emission intensity. To the best of our knowledge, this is the first time that such medically approved ceramic implants were characterized using PL-QY spectroscopy, revealing a strong fluorescent emission reaching far into the NIR-I optical bio-transparency window for BioloX delta.

2.2. Synthesis of Fluorescent ZTA using Flame-Spray Synthesis

Linking the obtained material characteristics to the photophysical properties does not yet conclusively explain why BioloX delta ZTA ceramics exhibit such strong fluorescence properties. However, the hypothesis of Cr-induced fluorescence^[23] in ZTA ceramics is supported by the detection of Cr via EDX in BioloX delta (0.3%) and BioloX forte (traces), and its absence or occurrence at non-detectable concentrations in the other ceramic femoral heads. To directly investigate the relationship between Cr-content and the fluorescence properties of ZTA ceramics, we developed a ZTA synthesis approach based on flame-spray-pyrolysis (FSP) that allows straightforward ZTA doping with ions, such as Cr. Metal-organic precursors were mixed at a desired elemental ratio, e.g., to obtain a ZTA with 80 % Al₂O₃ and 20 % ZrO₂ and optional dopants. The precursor solution was then fed through a spray nozzle and combusted in a methane/oxygen flame, allowing for the formation of the corresponding metal oxide particles, which were then collected on a filter paper mounted above the flame. As shown in Figure 3a, the obtained powder from this FSP process exhibited broad features characteristic of ZrO₂ in the XRD analysis, indicating small crystal sizes for ZrO₂ and a largely amorphous fraction of alumina. Subsequent sintering at 1200 °C led to the formation of t-ZrO₂, while calcination at 1400 °C finally yielded α -Al₂O₃ and t-ZrO₂ pattern characteristic of ZTA. Rietveld refinement further revealed the successful synthesis of ZTA with the expected ratio of Al₂O₃ to ZrO₂ of 8:2. Doping these structures with Cr did not lead to a detectable Cr₂O₃ signal in XRD (see Supporting Information Figure S5); however, the Cr-doping was confirmed via EDX. Using this straightforward synthesis approach, ZTAs with different Cr-doping contents, ranging from 0 to 5 wt% [0.01, 0.05, 0.1, 0.5, 1, 2, 5 theoretical wt% Cr₂O₃ in ZTA] were obtained and subsequently photophysically characterized. The as-prepared FSP powder did not show any fluorescence emission; however, the FSP powders calcined at 1200 °C revealed interesting optical properties. As hypothesized, the emission intensity at 693 nm increased with Cr content up to 1% (Figure 3b); however, it diminished strongly for samples with 2% and 5% Cr₂O₃. Simultaneously, we observed a second emission band at 683 nm emerged with increasing Cr levels. In the case of the 2% Cr-doped sample, this feature even displays the highest emission peak (Figure 3b, upper left panel). For the ZTA samples sintered at 1400 °C, all samples (even the Cr-free ZTA) showed a characteristic emission at 693 nm (Supporting Information Figure S6). With increasing Cr content, new features appeared at 686 and 713–771 nm, overall improving the emission in the NIR-I (>700 nm; Supporting Information Figure S7). These spectral differences become clearly visible in the 2D excitation–

emission maps (Figure 3c), showing the absence of the 683 nm emission feature in the 1400 °C sintered ZTA, as well as its very narrow peak at 693 nm with a full-width at half-maximum of 6 nm. Interestingly, a similar emission profile was found for the commercial ZTA ceramic implant BioloX delta and the synthesized ZTA with 0.5% Cr sintered at 1400 °C (Figure 3d), further supporting our hypothesis of a Cr-induced fluorescence. To further quantitatively assess how Cr-doping affects emission intensity, PL-QY spectroscopy was performed on the FSP-produced post-processed ZTA powders (Figure 3e).

These results clearly highlight the role of Cr-doping in the emission intensity of ZTA. For the samples sintered at 1200 °C, the strongest emission was observed for doping of 1% Cr with 33.5% PL-QY of sintered ZTA. Samples sintered at 1400 °C showed a consistently high PL-QY level of up to 60.2% in a range of 0.05–1% Cr-doping. These results further indicate that not only the Cr content but also the sintering temperature and hence the crystallinity and particle size influence the QY. Based on the XRD analysis (Supporting Information Figure S5), the ZrO₂ crystal sizes increased from \approx 20 to \approx 60 nm, and the Al₂O₃ crystal sized from \approx 2 to \approx 80 nm when comparing sintering at 1200 and 1400 °C. Notably, a pink color also arises with increasing Cr content after sintering the ZTA at 1400 °C, similar to the appearance of BioloX delta (Figure 3f). Further SEM analysis confirmed the differences in particle size and morphology of the two different sintering variations, while the corresponding EDX mapping (Figure 3g and Supporting Information Figures S8 and S9) identifies the main chemical elements and a relatively homogeneous Cr distribution, colocalizing with Al (Supporting Information Figure S10). SEM/EDX further allowed the size evaluation of the 1400 °C sintered Al₂O₃ particles with 1% Cr, which showed a mean grain size of \approx 300 nm. Taken together, these data reveal a direct dependence of the fluorescence properties on the Cr content in ZTA.

The outlined FSP procedure yielded the desired crystal phases after thermal annealing, in agreement with available data on Al₂O₃ ceramics synthesized via FSP.^[53,54] However, to the best of our knowledge, for the first time, we correlate Cr-doping with effects on the luminescence and PL-QY of ZTA ceramics. It should be noticed though, that Cr-doping of Al₂O₃ alone is known in the materials science community to impact the emission in a concentration-dependent way.^[55,56] We furthermore conclude from the similar emission features observed for BioloX delta and the 0.5 wt% Cr-doped ZTA that, indeed, Cr-doping is responsible for the characteristic emission peak in the NIR. This matches the reported Cr₂O₃ concentration for BioloX delta of about 0.3 wt% considerably well, whereas the manufacturer originally adds Cr (Cr₂O₃) to enhance the hardness and mechanical properties of the ceramic material.^[57] Furthermore, these data indicate that particle size and crystal phase strongly influence the absolute PL-QY, given the significant increase between the as-synthesized and samples sintered at 1200 and 1400 °C, respectively. BioloX delta fragments exhibited even a greater PL-QY, together with larger sintered Al₂O₃ domains as detected by SEM, overall supporting this hypothesis. This ZTA synthesis methodology could be used in the future to evaluate the effect of other dopants (Fe³⁺, Mn⁴⁺, Ti³⁺) and doping concentration on the NIR fluorescence emission, paving the way for ceramics with optimized luminescence properties.

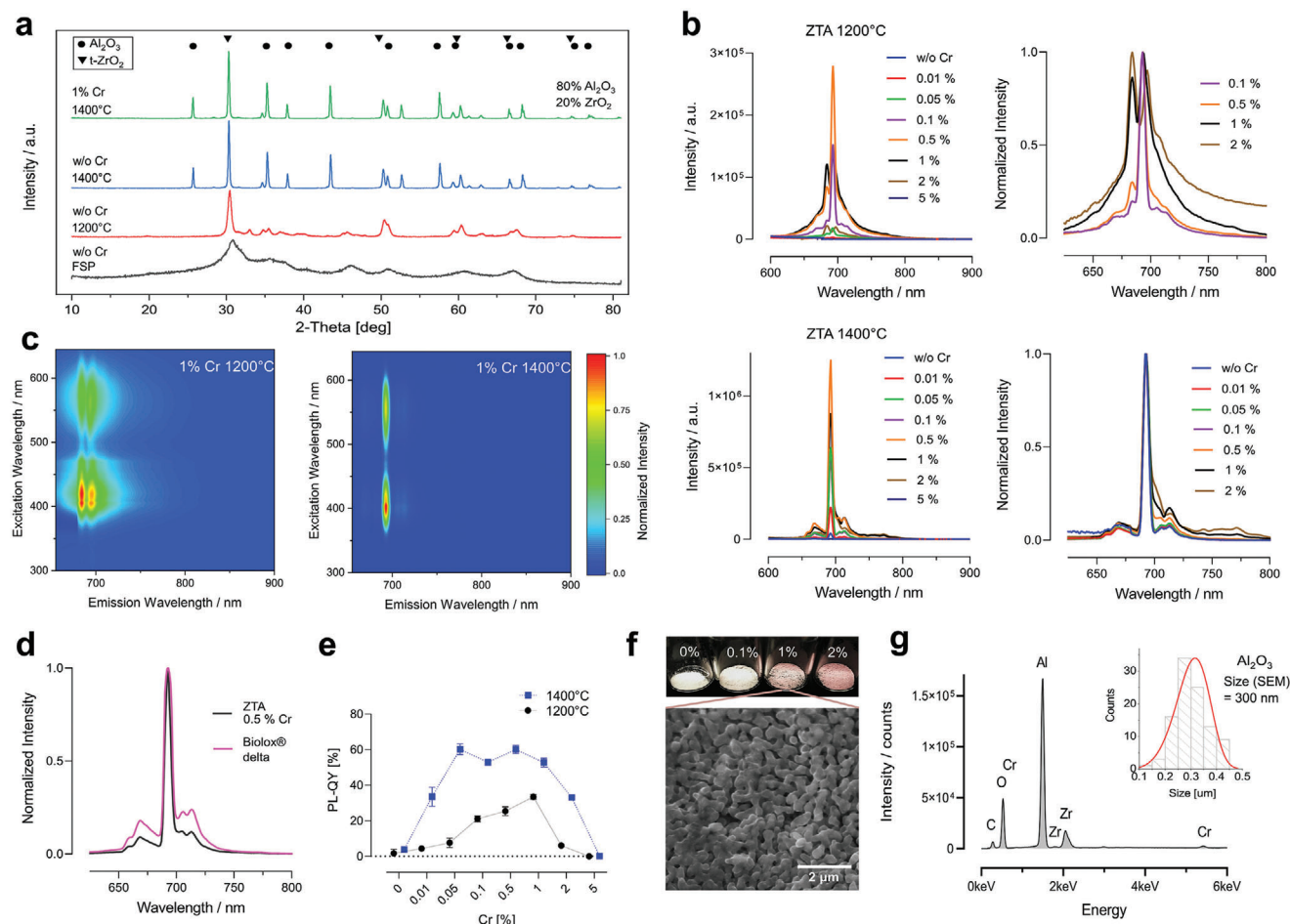


Figure 3. Synthesis of NIR-luminescent ZTA ceramics. a) XRD analysis of ZTA ceramics synthesized via FSP and temperature-dependent calcination. Rietveld refinement of the 1400 °C sintered sample revealed the desired composition of 80% Al_2O_3 and 20% ZrO_2 . b) Fluorescence spectra (upper panel, left) of ZTA sintered at 1200 °C show a Cr-content-dependent emission intensity (Cr [%] given as theoretical Cr_2O_3 content). Differences in the fluorescence profile become visible in the normalized fluorescence emission spectra (upper panel, right). Fluorescence spectra (lower panel, left) of ZTA sintered at 1400 °C follow a Cr-dependent emission intensity and increasing NIR tail (>700 nm) as seen in the normalized fluorescence emission spectra (lower panel, right). c) Excitation–emission maps of ZTA doped 1% Cr sintered at 1200 °C (left) and 1400 °C (right). d) Normalized fluorescence emission of commercial ZTA ceramic implant BioloX delta and synthesized ZTA with 0.5% Cr sintered at 1400 °C. e) PL-QY highly depends on the Cr content (theoretical wt% Cr_2O_3 in ZTA) as well as the sintering temperature (crystal/particle size). f) Photographs of ZTA powder show an increasingly strong pink color with increasing Cr content. Secondary electron (SE) image visualizes the morphology of sintered Al_2O_3 particles (1400 °C), while the corresponding EDX spectrum g) provides information on the main chemical constituents. Insert shows the histogram size distribution of the Al_2O_3 particles obtained from particle-size analysis based on SE images ($N = 100$).

2.3. NIR-Fluorescence Guides Fragment Detection

To exploit the aforementioned optical properties of widely implanted ZTA femoral heads, a camera-based detection method was established, enabling the remote visualization of potential splinters. We assembled a setup (Figure 4a,b) consisting of a camera (CMOS or InGaAs), an optical filter wheel (various long-pass (LP) emission filters) and, a light source (532 nm green laser, 638 nm red laser, and a light-emitting diode (LED) torch). Ceramic fragments of the above-mentioned femoral heads were placed below the filter wheel and imaged through avian (chicken) or hemoglobin-rich bovine tissue at well-defined tissue depths.

In accordance with our results from the PL (Figure 1d) and PL-QY characterization, only BioloX delta fragments were readily

detectable through 2 mm of tissue phantom (Figure 4a). Therefore, further experiments were carried out only with BioloX delta fragments. An exemplary series of NIR fluorescence images of a BioloX delta fragment, visualized through varying tissue phantom thicknesses, is shown in Figure 4c. As the dynamic range of the camera was limited (e.g., 8 or 16-bit), the exposure time needed to be adjusted to not saturate the image when imaging through increasing tissue depth. Independent of the equipped camera and filter settings, the pixel intensity scaled linearly with increased exposure time (Supporting Information Figure S11), allowing for robust detection at the higher integration times needed for deep tissue imaging. Figure 4d summarizes the required exposure times to reach a relative minimum mean pixel intensity of $I = 20$, dependent on the applied LP emission

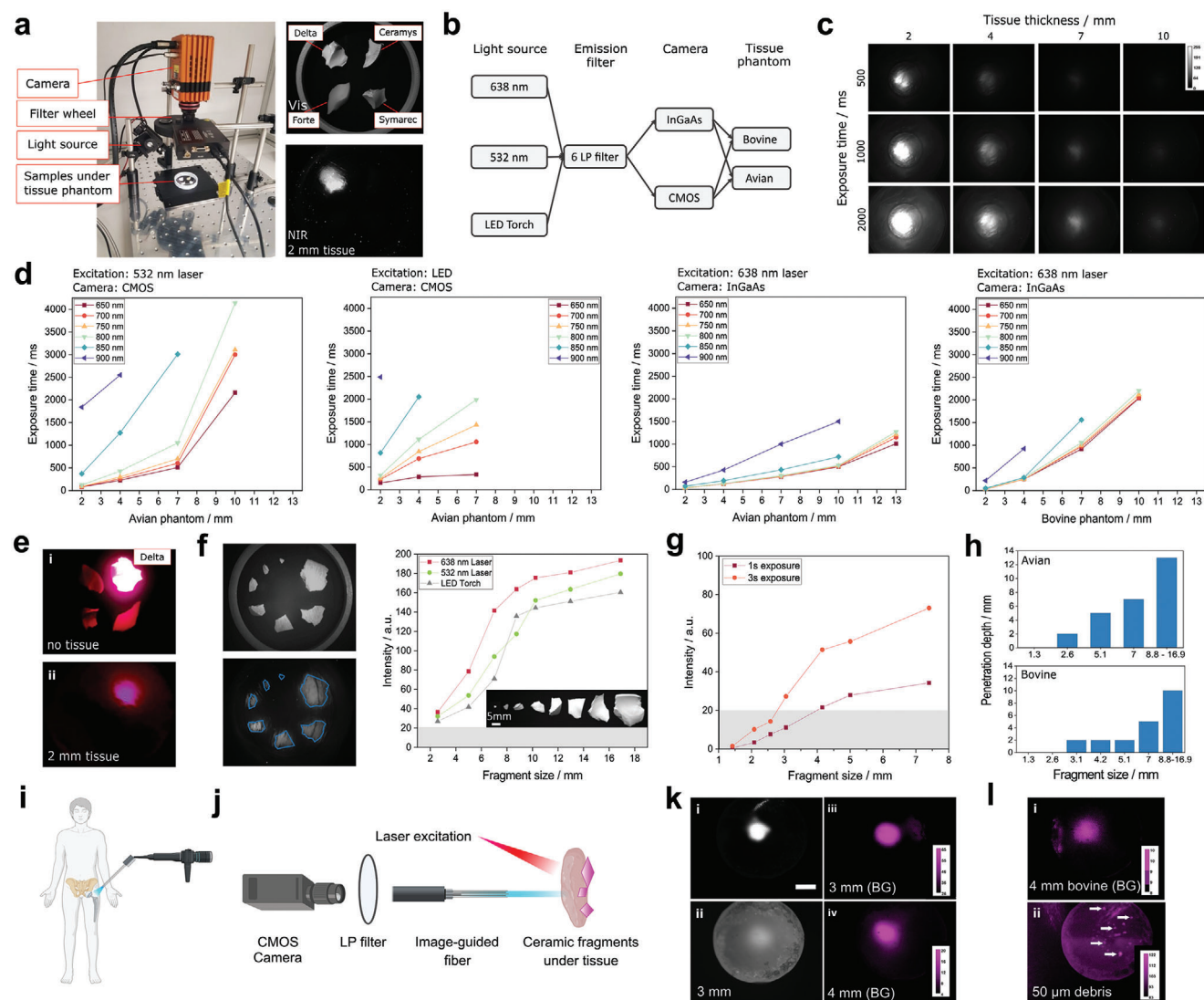


Figure 4. Remote NIR fluorescence detection of ceramic splinters. a) Optical setup for camera-based ceramic implant splinter identification (20 cm sample distance). Visible (Vis) photograph of the four ceramic types and their corresponding NIR-fluorescence image through 2 mm of tissue phantom. b) Schematic representation of the measurement conditions, evaluating the optimal detection method, as well as its capabilities to detect ceramic fragments of different sizes through avian and bovine tissue phantom. c) Representative series of a 17 mm large delta fragment imaged through avian tissue phantom (532 nm excitation, 700 nm LP, CMOS camera). d) Evaluated exposure time to reach a relative intensity value ($I = 20$, 8-bit image), as a threshold for distinct fluorescence identification. A combination of varying the camera, excitation light source, LP emission filter, and tissue phantom (thicknesses) is indicated before exceeding a maximal integration time of 10 s. e) Proof-of-principle detection of Biologix delta fragments using a smartphone camera and a 650 nm LP filter i) without and ii) through 2 mm of avian phantom. f) Evaluation of detectable fragment sizes through 2 mm of avian phantom (InGaAs camera, 1 s integration time, 700 nm LP) and in (g) for smaller fragments through bovine tissue (638 nm excitation). h) Maximal penetration depth through avian and bovine tissue phantom versus Biologix delta ceramic fragment size for the tested InGaAs camera. i) Schematic for arthroscopy-based hip arthroscopy examination. j) Setup for the arthroscopy prototype where an image-guided fiber transfers the fluorescence image to a CMOS camera. k) Fluorescence images captured via the image-guided arthroscopy fiber. i) Image of a 0.8×0.8 mm sized Biologix delta splinter. ii) Same splinter under 3 mm of chicken tissue phantom. iii) Background correction and thresholding clearly identify the ceramic splinter. iv) Fluorescence image of the splinter under 4 mm of chicken tissue phantom. l) i) Fluorescence image of the splinter under 4 mm bovine-phantom. ii) 50–70 μ m sized ceramic debris (while arrows) visualized using image-guided arthroscopy.

filter and tissue thickness (see also Supporting Information Figure S12). The most efficient imaging settings were obtained using the 532 nm laser-diode for excitation and a CMOS camera for detection and the 638 nm laser-diode in combination with the InGaAs-Camera, resulting in a maximal penetration of chicken tissue phantom of 10 and 13 mm, respectively. Ceramic emission

after excitation using white LED light was equally well detected by both cameras, allowing a stand-up detection of up to 7 mm. When using bovine tissue, a reduced penetration depth of 10 mm was achieved using the 638 nm laser-diode and an InGaAs camera. A detailed analysis can be found in Supporting Information Figure S13. For all tested LP emission filters, it became apparent

that longer integration times were necessary when imaging in the NIR emission tail. The best results were obtained for the detection using the CMOS camera with a 650–750 nm LP filter, while the InGaAs camera showed near equal results for filter settings up to 800 nm. Moreover, in a proof-of-concept experiment, such ceramic fragments could also be detected using a standard smartphone camera equipped with a 650 nm LP filter (Figure 4e). To assess the limitations of these settings in terms of detectable fragment size and imaging time, small BioloX delta fragments between 2.6 and 6.9 mm were placed under a 2 mm chicken tissue phantom (Figure 4f and Supporting Information Figure S14). All tested fragments could be identified within an integration time of 1 s, regardless of the used optical settings (Supporting Information Figure S15). A second set of fragments within the clinically most relevant size range (1.5–7.5 mm; see Supporting Information Figure S16) was investigated under the bovine phantom. This fragment size evaluation is based on the image analysis of retrieved heads and liners from previous publications^[58–61] with a total of 95 splinters (Supporting Information Figure S16). Fragments larger than 3 mm could easily be visualized, whereas smaller fragments showed mean pixel intensities of <20; however, they were still detectable via image postprocessing. Consequently, we concluded that the camera-based detection approach can at least identify fragments >2.6 mm under 2 mm of avian tissue as well as 3.1 mm fragments under 2 mm of hemoglobin-rich bovine tissue.

For intraoperative detection and the identification of even smaller fragments, an arthroscopy setup was developed (Figure 4i). In the first prototype of such a device, an image-guided fiber transmits the fluorescence information to a standard CMOS camera (Figure 4j). This allowed the clear identification of sub-millimeter-sized fragments (800 μ m), even under up to 4 mm of avian tissue phantom (Figure 4k) and 4 mm of bovine tissue phantom (Figure 4l). Moreover, even 50–70 μ m sized debris-like particles were identified in a blood-containing artificial synovial background in a straightforward manner. This outlines the promising capabilities such an arthroscopy setup can offer for the in situ detection of potential debris or the ionizing radiation-free identification of small fragments within tissue during hip revision surgery. Currently, the removal of ceramic debris is mainly based on the technical skills of the orthopedic surgeon; hence, frequently associated with the lavish removal of surrounding capsule tissue. Established methods, such as the intraoperative use of fluoroscopy as a planar X-ray technique, have limited success in identifying fragments within the correct tissue layer.^[62] The fluorescence-based detection approach offers a standardized way for precision surgery, suitable for the hybrid operating room in the future.

The presented image-guided detection approach enables the direct, label-free detection of fragments and debris of the most widely used commercial implants. Based on the efficient detection of the ceramic fluorescence with an 800 nm LP-filter set, no specialized InGaAs cameras are generally required. Consequently, the NIR imaging of debris can be realized with comparably inexpensive CMOS cameras (<1000\$) and the technique could be straightforwardly implemented into clinical routine without major regulatory hurdles. And as fluorescence-based image-guided surgery is on the rise for tumor removal,^[63] a similar technique could be applied for the removal of ceramic frag-

ments. In situations where an improved tissue penetration, as well as better signal-to-noise ratio during imaging is needed, one could imagine that next-generation cameras will enhance the benefits achievable with NIR imaging. Moreover, recent advantages in imaging modalities can even allow for depth-resolved stereo vision.^[64] This said, the general improvements in optical equipment will enable enhanced resolution and signal-to-noise ratios, with decreasing costs in the future. As outlined in Supporting Information Figure S16, we aimed to test the imaging approach with the clinically most relevant fragment sizes. Here, the camera-based imaging system (20 cm distance to the sample) was able to detect fragments of down to \approx 2 mm in size below 2 mm of tissue phantom, which corresponds to 92% of all clinically relevant splinters. However, we cannot exclude the formation of smaller fragments (<2 mm) as only sparse reports are available on clinically observed fragment sizes, which furthermore do not specify the size fraction of splinters that might remain in the joint tissue, upon incomplete revision surgery. Smaller splinters could, however, be directly detected with the introduced arthroscopy prototype (Figure 4i), which is able to detect sub-mm fragments even under several mm thick tissue phantoms. This technique holds great promise, offering multiple possibilities for arthroscopic evaluation, such as detecting wear formation in a minimally invasive manner.

2.4. Ceramic Debris Detection via Fluorescence Microscopy

In addition to the fluorescence-based visualization of macroscopic fragments, the same principles can be applied to detect potential ceramic debris (wear particles), typically arising from wear and tear. For such purposes, commercial microscopy equipment can be modified to detect ceramic PL emissions (Figure 5a). This low-cost (\approx 500\$) extension includes a 650 nm short-pass (SP) filter in the direction of the excitation light source, a 638 nm dichroic mirror, and a 650 nm LP filter before the emitted light is detected using a standard camera (CCD detector). In such a way, it is possible to detect BioloX delta debris down to μ m-sized particles (Supporting Information Figure S17). To demonstrate multichannel fluorescence detection, fixed fibroblast cells were stained and imaged in an artificial synovial fluid background containing the ceramic debris. The different emission channels, here the cytoplasm was visualized using Alexa Fluor 488 Phalloidin staining and the cell nucleus via 4',6-diamidino-2-phenylindole (DAPI) staining, are not affected by the ceramic signal and vice versa (Figure 5b). Moreover, even in complex matrices, such as blood, the detection of micrometer-sized ceramic particles can be achieved in a straightforward manner (Figure 5c). Although such ceramic implants are known for their high durability and low abrasion, wear particle formation on, e.g., CoC bearings cannot be entirely prevented. This developed detection approach could offer an easy, fast, and cost-effective route to visualize ceramic particles in body fluid (synovial fluid), e.g., collected by joint aspiration as well as in histological specimens (joint capsules). Until now, labor-intensive techniques, such as SEM, with a vastly limited field of view, were needed to identify ceramic debris in biological environments, such as joint tissue.^[65] The introduced NIR fluorescence-based detection holds great promise to visualize even sub- μ m-sized

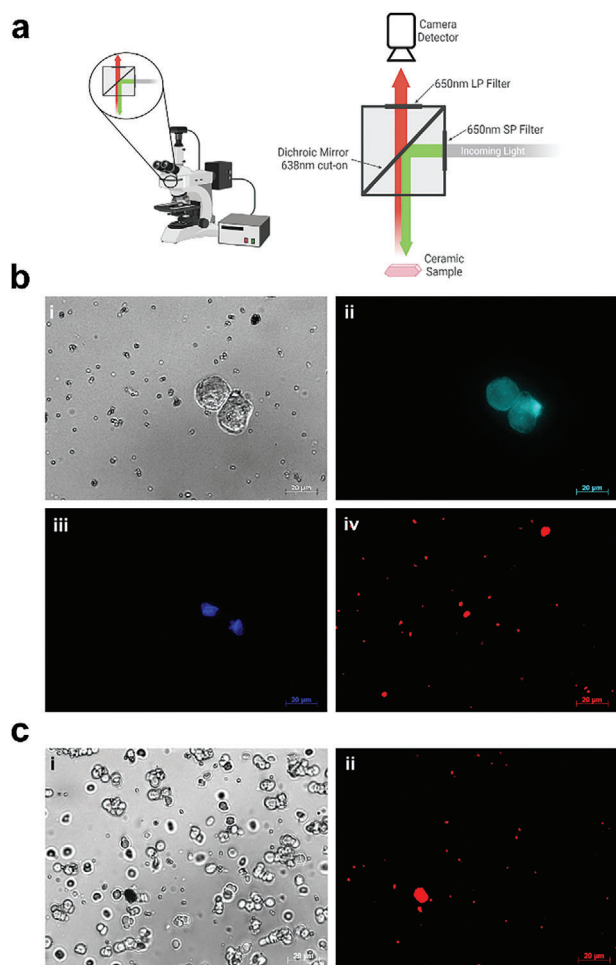


Figure 5. Ceramic debris detection using NIR fluorescence microscopy. a) Modification of a commercial fluorescence microscope allows for the detection of BioloX delta ceramic particles. Excitation light is filtered using a 650 nm SP filter and reflected using a 638 nm cut-on dichroic mirror toward the sample. The emitted light is transmitted through a 650 nm LP filter until it is detected by a standard CCD camera. b) Proof-of-concept visualization of ceramic debris in artificial synovia background containing fixed, stained fibroblast cells. i) Brightfield; ii) Alexa Fluor 488 staining; iii) DAPI staining; iv) ceramic fluorescence. c) Detection of ceramic debris in a blood background. i) Brightfield (with blood platelets); ii) ceramic fluorescence.

particles, approaching the optical resolution limit by fluorescence microscopy.^[66]

Due to its easy accessibility, this technique can be readily used to study the interaction of ceramic debris on a cellular level (e.g., uptake or translocation) or to detect debris in histology samples. Moreover, based on the unique fluorescence signature of the ceramic debris, it could potentially be detected directly via flow cytometry or fluorescence-activated cell sorting (FACS) analysis. These analyses are commonly used to identify increased amounts of (immune) cells within the synovial fluid as a marker for periprosthetic joint infections.^[67,68] Wear debris can falsify the readout signal, so a correction for potential wear debris based on the ceramic-intrinsic fluorescence signal holds great promise in improving diagnostic accuracy. Additionally, in-

creased detection of debris after joint fluid aspiration could be used as a marker for aseptic loosening.^[69,70] With increasing availability of NIR detectors in commercial flow cytometry or FACS devices,^[71,72] we expect that such analysis will become routinely accessible, presumably also to detect fluorescent ceramic debris.

2.5. Conclusions and Outlook

Most currently performed hip arthroplasties use a bearing combination based on ceramic cups, favored because of their high strength and low abrasion. However, a small fraction of implanted ceramics fracture within their lifetime, leading to severe orthopedic complications.^[13] Both ceramic fragmentation and excessive implant wear might require complex and challenging hip revision surgery; however, current capabilities for intraoperative visualization of fragments are limited. Here, we harness the material-intrinsic PL properties to establish an image-guided surgical approach for the direct, label-free visualization of implant fragments and wear. This presents an elegant approach both from a materials science perspective as well as from a surgical point of view. Proceeding from the optical characterization of clinically established ceramic hip implants, we identified BioloX delta as ZTA ceramic with a pronounced fluorescence emission around 690 nm. This emission feature was characterized using PL-QY spectroscopy showing an optimal excitation at 420 and 560 nm, with an overall PL-QY of 74%. Notably, the emission feature reached into the NIR-I until 1000 nm, forming a prerequisite for fluorescence imaging in the NIR biological transparency window. Further chemical analysis of the different ceramics used in commercial implants revealed significant differences in Cr content, presumably the origin of the distinct luminescence properties. Hence, ZTAs with varying Cr concentrations were synthesized via FSP and subsequently sintered to obtain the desired ZTA crystal phases. Upon studying their photoluminescent properties, the effect of Cr-doping became apparent, revealing an emission at ≈ 690 nm with intensifying features in the NIR range with increasing Cr content (expressed as wt% Cr_2O_3 in ZTA, with 80% Al_2O_3 and 20% ZrO_2). Such ZTA ceramics sintered at 1400 °C with 0.05–1% Cr showed a PL-QY of up to 60%. The presented FSP-based synthesis of fluorescent ZTA can be used to directly tailor the photoluminescent properties of implant ceramics in the future, beyond femoral heads to dental implants. Chemical and optical characterization displayed the potential for the developed remote NIR fluorescence detection approach, identifying a combination of red (638 nm) laser excitation and imaging via an InGaAs camera as most suitable for mm-sized ceramic (BioloX delta) fragment detection, even under several mm of tissue. The technique works almost equally well when using an inexpensive CMOS camera, resulting in a splinter-size-dependent penetration depth of the ceramic fluorescence signal. To highlight the feasibility of an interoperative application, an arthroscopy prototype was developed, transmitting the NIR fluorescence via an image-guided fiber. This allowed for sub-mm-sized splinter detection, even under 4 mm of (avian or bovine) tissue phantom. Lastly, a microscopy-based ceramic debris detection approach is introduced, utilizing a commercial fluorescence microscopy setup with low-cost extension of the

optical elements. This allows for the detection of debris-like ceramic particles down to the sub- μm -range, only restricted by the optical resolution limit. Hence, NIR-imaging has the potential to become a straightforward visualization technique for ceramic particles within complex biological environments such as synovial fluid or histological specimens.

Taken together, the outlined approach capitalizes on the material-intrinsic properties of ceramic hip implants, demonstrating that Cr-dopants in commercial ZTA implants give rise to NIR fluorescence with a high absolute quantum yield that can be employed for noninvasive, radiation-free imaging. This allows the NIR-fluorescence-based detection of macroscopic and microscopic ceramic fragments of some of the most widely implanted ceramics (BioloX delta). As by the year 2017, over 7 million components^[73] made of BioloX delta (5.5 million ball heads, more than 2 million inserts) are implanted and numbers are continuously rising,^[4,5,14] we expect the outlined approach is applicable already in thousands of clinical cases. Nonetheless, not all commercial ceramic implants contain significant dopant-levels, hence possess strong fluorescence emission, and further improvements may be needed to also address these segments. As the fluorescence quantum yield of BioloX forte was identified with 8% and Symarec with 1%, further optimization of the optical detection technique could allow for microscopic, potentially even camera-assisted ceramic splitter detection. Overall, by harnessing the NIR fluorescent properties of ZTA implant ceramics, we aim to overall make this highly advanced material even more safe and applicable in the future. As the approach is based on the material-intrinsic properties of the most widely implanted hip cup ceramics, this low-cost imaging approach can be readily implemented into clinical routines without any major regulatory hurdles. Because the approach does not rely on ionizing radiation, it may pave the way to precision extraction of fragments in a considerably less traumatic, tissue-sparing, and minimally invasive approach.

3. Experimental Section

Unless otherwise stated, all materials were purchased from Sigma Aldrich.

Ceramic Implants: Ceramic heads were provided by the University Hospital Cologne, Department of Orthopedics, Traumatology and Reconstructive Surgery (Cologne, Germany) and the Deutsches Zentrum für Orthopädie, Department of Orthopaedics and Trauma Surgery (Eisenberg, Germany), either obtained from revision surgery or newly purchased as indicated. For fragment visualization experiments, heads were then broken by mechanical force. Splinters were further processed into powder, for later chemical characterization and to mimic ceramic debris/wear particles (Retsch mixer mill MM400, 35 mL ZrO grinding jars and \varnothing 1 cm ZrO grinding balls; 1 min 20 s at 25 Hz).

XRD: XRD analysis was performed with a Bruker D2 2nd Gen Phaser (30 kV, 10 mA, SSD160 detector, Cu tube 1.54184 Å) $K\alpha$ radiation at $2\theta = 10^\circ$ – 80° with a step size of 0.01° . Phase composition and crystallite sizes were determined using the Diffraction Eva (V3.1) software, after performing Rietveld parameter refinement.

SEM: SEM with EDX was performed on an Axia Chemisem (Thermo Fisher, NL). Samples were coated with 10 nm carbon (Leica EM ACE600) prior to analysis.

Fluorescence Spectroscopy: 1D and 2D excitation–emission fluorescence spectra were obtained using a Spectrofluorometer F55 (Edinburgh Instruments, SC-15 front face sample holder, Photomultiplier R928P emis-

sion detector). Typically, 1D spectra were recorded with 1 nm step width and an integration time of 0.1 s. 2D excitation–emission spectra in the VIS were recorded in 5 nm steps of 0.4 s dwell time. NIR fluorescence emission spectra were recorded with a Shamrock 193i spectrometer equipped with an InGaAs detector (Andor Technology Ltd., Belfast, Northern Ireland) using a 561 nm Cobolt Jive laser (Cobolt AB, Solna, Sweden) as excitation source. A monochromator (MSH150 instrument, equipped with a LSE341 light source, LOT-Quantum Design GmbH, Darmstadt, Germany) was used for excitation (5 nm steps) to obtain 2D-NIR excitation–emission spectra.

Quantum Yield Spectroscopy (PL-QY): Absolute PL-QY spectroscopy was performed with a Hamamatsu Quantarus-QY (C11347) using solid phase quartz glass sample holders. Excitation scan regime was set to 400–650 nm (5 nm steps), while area to detect all emitted photons was adjusted to cover the entire emission, e.g., for BioloX delta samples to 640–830 nm.

Remote NIR Fluorescence Camera-Based Detection: In a home-built optical system, two different cameras (CMOS and InGaAs) were compared for imaging performance. The Ninox SWIR 640 uses an SCD Sensor (InGaAs PIN-Photodiode) with a spectral response of 400–1700 nm, was connected through an EPIX mf2280–C frame grabber, while images were recorded using the EPIX XCAP V3.8 software. Basler acA1920-40 μm used an IMX249 Sensor (CMOS) and had a spectral response of 400–1000 nm. Both cameras were used with a StingRay Optics 25 mm SWIR SR2343-A01 lens. All images were analyzed using the ImageJ 1.51s software. As excitation light, three different sources were tested. A green laser (532 nm, 200 mW (measured power: 116 mW cm^{-2}), TopLaser Store green laser with TTL modulation), a red laser (638 nm, 750 mW (measured power: 498 mW cm^{-2}), TopLaser Store orange-red laser with multimode diode laser, PWM/TTL modulation), and a white light LED torch (Asort LED torch, 25 000 Lumen, measured power: 248 mW). Besides the cameras and light sources, the set up additionally used the following optical components: a diffuser (220 Grit Ground Glass Diffuser (Thorlabs, DG10-220)) in front of the lasers, a 1000 nm SP filter in front of the camera lens, and a motorized filter wheel (Thorlabs 6-Position Motorized Filter Wheel, FW102C) containing six different LP filters ranging from 650 to 900 nm (FELH0650/FELH0700/FELH0750/FELH0800/FELH0850/FELH0900, Thorlabs, round 25 mm). For the fragment visualization experiments, a tissue phantom (avian or bovine) was prepared with 2–3 mm thickness each, while stacking created a phantom of varying thicknesses.

Microscopy: Wear particle imaging was performed with a Zeiss AxioImager.M2m fluorescence microscope. The microscope was equipped with two different light sources: a white light halogen lamp (Hal100) and a set of LEDs at different wavelengths: 365, 470, and 530 nm (Colibri.2). The samples were imaged using bright field or dark field filter sets, respectively, with a DAPI filter set (BP 365/12 nm, DM 395 nm, LP 397 nm) or the Fluo-3 filter set (BP 475/25 nm, DM 550 nm, BP 510/25 nm) for cell visualization. Imaging of the fluorescent ceramic particles, a custom filter set was developed using a 650 nm SP filter, a 638 nm dichroic mirror, and a 650 nm LP filter (Thorlabs). To image the powder particles with different backgrounds, a synovial fluid mimic (3 g L^{-1} hyaluronic acid in Ringer lactate buffer with 30 g L^{-1} bovine serum albumin) containing stained, fixed fibroblasts cells (DAPI and Alexa Fluor 488 Phalloidin) as well as pig blood samples were tested.

ZTA Synthesis via FSP: Nanomaterials were synthesized via liquid-fed FSP, injecting 5 mL min^{-1} metal-organic precursor solution into a CH_4/O_2 (1.5:3.2 L min^{-1}) flame, dispersed by 5 L min^{-1} O_2 stream. Aluminium(III)-acetylacetonat was dissolved in tetrahydrofuran under stirring, while zirconium(IV) propoxide solution was added to obtain a total ion metal concentration of 0.3 M, aiming for a final composition of 80% Al_2O_3 and 20% ZrO_2 . Varying amounts of chromium(III) nitrate nonahydrate were dissolved in iso-propanol and added under stirring, to match a desired Cr (wt% Cr_2O_3 in ZTA) concentration. Particles were subsequently collected on a glass fiber filter mounted 60 cm above the flame. ZTA nano powder was then calcified at 1200 $^\circ\text{C}$ for 2 h at ambient atmosphere (Sintering furnace Type 4800, Thermolyne) or at 1400 $^\circ\text{C}$ for 20 min, using a thermogravimetric analysis (METTLER TOLEDO TGA/DSC 3+; 25 K min^{-1} ramp; 40 mL min^{-1} air flow).

Supporting Information

Supporting Information is available from the Wiley Online Library or from the author.

Acknowledgements

The authors want to express their sincere gratitude to Prof. Sebastian Kruss, for access to the NIR-set up. Furthermore, the authors thank Stephan Wartenweiler and Negar Haghipour for their help milling the ceramic implant samples and Dr. Lukas Gerken for cell cultivation. This work was supported by an ETH Career Seed Award funded through the ETH Zurich Foundation (R.N.) and by the Swiss National Science Foundation (Eccellenza grant no. 181290) (I.H.).

Open access funding provided by Eidgenössische Technische Hochschule Zurich.

Conflict of Interest

The authors declare no conflict of interest.

Data Availability Statement

The data that support the findings of this study are available from the corresponding author upon reasonable request.

Keywords

Al₂O₃, bioimaging, ceramic implant, luminescent ceramics, NIR fluorescence, ruby, zirconia-toughened alumina, ZTA

Received: September 4, 2023

Revised: January 10, 2024

Published online:

- [1] I. D. Learmonth, C. Young, C. Rorabeck, *Lancet* **2007**, 370, 1508.
- [2] H. M. Kremers, D. R. Larson, C. S. Crowson, W. K. Kremers, R. E. Washington, C. A. Steiner, W. A. Jiranek, D. J. Berry, *J. Bone Jt. Surg., Am. Vol.* **2014**, 97, 1386.
- [3] R. Pivec, A. J. Johnson, S. C. Mears, M. A. Mont, *Lancet* **2012**, 380, 1768.
- [4] *American Joint Replacement Registry (AJRR): 2023 Annual Report*, American Academy of Orthopaedic Surgeons (AAOS), Rosemont, IL **2023**.
- [5] C. Pabinger, H. Lothaller, N. Portner, A. Geissler, *HIP Int.* **2018**, 28, 498.
- [6] J. A. Singh, S. Yu, L. Chen, J. D. Cleveland, *J. Rheumatol.* **2019**, 46, 1134.
- [7] C. Y. Hu, T. R. Yoon, *Biomater. Res.* **2018**, 22, 33.
- [8] J. P. Garino, *Semin. Arthroplasty: JSES* **2011**, 22, 214.
- [9] P. Hernigou, S. Zilber, P. Filippini, A. Poignard, *Clin. Orthop. Relat. Res.* **2009**, 467, 2274.
- [10] T. Bouras, T. Repantis, P. Fennema, P. Korovessis, *Eur. J. Orthop. Surg. Traumatol.* **2014**, 24, 1439.
- [11] A. Hatton, J. E. Nevelos, A. A. Nevelos, R. E. Banks, J. Fisher, E. Ingham, *Biomaterials* **2002**, 23, 3429.
- [12] C. Esposito, F. Maclean, P. Campbell, W. L. Walter, W. K. Walter, S. F. Bonar, W. R. Walsh, J. Norman, *J. Arthroplasty* **2013**, 28, 860.
- [13] P. Massin, R. Lopes, B. Masson, D. Mainard, *Orthop. Traumatol. Surg. Res.* **2014**, 100, S317.
- [14] G. Hallan, A. M. Fenstad, O. Furnes, *Clin. Orthop. Relat. Res.* **2020**, 478, 1254.
- [15] G. C. Lee, R. H. Kim, *J. Arthroplasty* **2017**, 32, 546.
- [16] S. Stea, F. Traina, A. Beraudi, M. Montesi, B. Bordini, S. Squarizoni, A. Sudanesse, A. Toni, *J. Orthop. Res.* **2012**, 30, 1312.
- [17] O. Kocadal, T. Ozler, A. E. T. Bolukbasi, F. Altintas, *Hip Pelvis* **2019**, 31, 124.
- [18] C. Im, K.-J. Lee, B.-W. Min, K.-C. Bae, S.-W. Lee, H.-J. Sohn, *Hip Pelvis* **2018**, 30, 156.
- [19] M. Izerrouken, Y. Djouadi, H. Zirour, *Nucl. Instrum. Methods Phys. Res., Sect. B* **2014**, 319, 29.
- [20] R. Krishnan, S. Dash, R. Kesavamoorthy, C. Babu Rao, A. K. Tyagi, B. Raj, *Surf. Coat. Technol.* **2006**, 200, 2791.
- [21] K. G. Dassios, C. Galotis, *Appl. Phys. A: Mater. Sci. Process.* **2004**, 79, 647.
- [22] G. Pezzotti, T. Tateiwa, W. Zhu, T. Kumakura, K. Yamada, K. Yamamoto, *J. Biomed. Opt.* **2006**, 11, 024009.
- [23] S. Adachi, *Opt. Mater.* **2021**, 114, 111000.
- [24] R. C. Powell, B. Dibartolo, *Phys. Status Solidi* **1972**, 10, 315.
- [25] T. H. Maiman, *Nature* **1960**, 187, 493.
- [26] R. F. Cook, C. A. Michaels, *J. Res. Natl. Inst. Stand. Technol.* **2017**, 122, 43.
- [27] J. A. Pardo, R. I. Merino, V. M. Orera, J. I. Peña, C. González, J. Y. Pastor, J. Llorca, *J. Am. Ceram. Soc.* **2000**, 83, 2745.
- [28] G. C. Brown, *J. Appl. Phys.* **1964**, 35, 3062.
- [29] L. Trinkler, B. Berzina, Z. Jevsjutina, J. Grabis, I. Steins, C. J. Baily, *Opt. Mater.* **2012**, 34, 1553.
- [30] V. N. Snytnikov, V. O. Stoyanovskii, T. V. Larina, O. P. Krivoruchko, V. A. Ushakov, V. N. Parmon, *Kinet. Catal.* **2008**, 49, 291.
- [31] C. Pflichtsch, R. A. Siddiqui, B. Atakan, *Appl. Phys. A: Mater. Sci. Process.* **2008**, 90, 527.
- [32] A. Rastorguev, M. Baronskiy, A. Zhuzhgov, A. Kostyukov, O. Krivoruchko, V. Snytnikov, *RSC Adv.* **2015**, 5, 5686.
- [33] Y. Xu, L. Wang, B. Qu, D. Li, J. Lu, R. Zhou, *J. Am. Ceram. Soc.* **2019**, 102, 2737.
- [34] C. Tian, H. Lin, D. Zhang, P. Zhang, R. Hong, Z. Han, X. Qian, J. Zou, *Opt. Express* **2019**, 27, 32666.
- [35] M. Grinberg, A. Mandelis, K. Fjeldsted, A. Othonos, *Phys. Rev. B* **1993**, 48, 5922.
- [36] V. B. Mikhailik, H. Kraus, D. Wahl, M. S. Mykhaylyk, *Appl. Phys. Lett.* **2005**, 86, 101909.
- [37] G. Hong, A. L. Antaris, H. Dai, *Nat. Biomed. Eng.* **2017**, 1, 0010.
- [38] Y. Chen, S. Wang, F. Zhang, *Nat. Rev. Bioeng.* **2023**, 1, 60.
- [39] G. Selvaggio, R. Nißler, P. Nietmann, A. Patra, L. J. Patalag, A. Janshoff, D. B. Werz, S. Kruss, *Analyst* **2022**, 147, 230.
- [40] J. Cao, B. Zhu, K. Zheng, S. He, L. Meng, J. Song, H. Yang, *Front. Bioeng. Biotechnol.* **2020**, 7, 487.
- [41] J. Pan, F. Li, J. H. Choi, *J. Mater. Chem. B* **2017**, 5, 6511.
- [42] R. Nißler, J. Ackermann, C. Ma, S. Kruss, *Anal. Chem.* **2022**, 94, 9941.
- [43] G. Selvaggio, A. Chizhik, R. Nißler, I. Kuhlemann, D. Meyer, L. Vuong, H. Preiß, N. Herrmann, F. A. Mann, Z. Lv, T. A. Oswald, A. Spreinat, L. Erpenbeck, J. Großhans, V. Karius, A. Janshoff, J. Pablo Giraldo, S. Kruss, *Nat. Commun.* **2020**, 11, 1495.
- [44] F. H. L. Starsich, P. Gschwend, A. Sergeev, R. Grange, S. E. Pratsinis, *Chem. Mater.* **2017**, 29, 8158.
- [45] F. Traina, M. De Fine, A. Di Martino, C. Faldini, *Biomed. Res. Int.* **2013**, 2013, 157247.
- [46] V. Sharma, A. S. Ranawat, V. J. Rasquinha, J. A. Weiskopf, H. Howard, C. S. Ranawat, *J. Arthroplasty* **2010**, 25, 342.
- [47] P. Bouvier, E. Djurado, G. Lucazeau, T. L. Bihan, *Phys. Rev. B: Condens. Matter Mater. Phys.* **2000**, 62, 8731.
- [48] F. Castelli, L. S. Forster, *J. Lumin.* **1974**, 8, 252.
- [49] A. Mandelis, Z. Chen, R. Bleiss, *Opt. Eng.* **1993**, 32, 2046.

- [50] R. S. Quimby, W. M. Yen, *J. Appl. Phys.* **1980**, *51*, 1780.
- [51] H. Tomaszewski, J. Strzeszewski, *Mater. Sci. Forum* **2002**, 404–407, 899.
- [52] R. F. Cook, C. A. Michaels, *J. Res. Natl. Inst. Stand. Technol.* **2017**, *122*, 43.
- [53] A. I. Y. Tok, F. Y. C. Boey, X. L. Zhao, *J. Mater. Process. Technol.* **2006**, *178*, 270.
- [54] L. D. Hafshejani, S. Tangsir, H. Koponen, J. Riikonen, T. Karhunen, U. Tapper, V. P. Lehto, H. Moazed, A. A. Naseri, A. Hooshmand, J. Jokiniemi, A. Bhatnagar, A. Lähde, *Powder Technol.* **2016**, *298*, 42.
- [55] G. C. da Cunha, C. M. Abreu, J. A. Peixoto, L. P. C. Romão, Z. S. Macedo, *J. Inorg. Organomet. Polym. Mater.* **2017**, *27*, 674.
- [56] Z. K. Heiba, M. B. Mohamed, A. M. Wahba, *J. Mater. Sci.* **2020**, *31*, 14645.
- [57] M. Kuntz, R. Krüger, *Ceram. Int.* **2018**, *44*, 2011.
- [58] J. L. Masonis, R. B. Bourne, M. D. Ries, R. W. McCalden, A. Salehi, D. C. Kelman, *J. Arthroplasty* **2004**, *19*, 898.
- [59] S. Stea, M. Visentin, B. Bordini, F. Traina, S. Squarzone, A. Toni, *Int. J. Artif. Organs* **2006**, *29*, 800.
- [60] Y. S. Park, S. K. Hwang, W. S. Choy, Y. S. Kim, Y. W. Moon, S. J. Lim, *J. Bone Jt. Surg.* **2006**, *88*, 780.
- [61] G. Maccauro, C. Piconi, W. Burger, L. Pilloni, E. De Santis, F. Muratori, I. D. Learmonth, *J. Bone Jt. Surg., Br. Vol.* **2004**, *86*, 1192.
- [62] C. Goretti, F. Polidoro, S. Paderni, A. Belluati, *Acta Biomed.* **2019**, *90*, 192.
- [63] K. Wang, Y. Du, Z. Zhang, K. He, Z. Cheng, L. Yin, D. Dong, C. Li, W. Li, Z. Hu, C. Zhang, H. Hui, C. Chi, J. Tian, *Nat. Rev. Bioeng.* **2023**, *1*, 161.
- [64] Q. Zhou, D. Nozdriukhin, Z. Chen, L. Glandorf, U. A. T. Hofmann, M. Reiss, L. Tang, X. L. Deán-ben, D. Razansky, *Adv. Sci.* **2023**, *10*, 2204782.
- [65] D. De Pasquale, S. Stea, A. Beraudi, M. Montesi, S. Squarzone, A. Toni, *J. Arthroplasty* **2013**, *28*, 838.
- [66] A. M. Edmonds, M. A. Sobhan, V. K. A. Sreenivasan, E. A. Grebenik, J. R. Rabeau, E. M. Goldys, A. V. Zvyagin, *Part. Part. Syst. Charact.* **2013**, *30*, 506.
- [67] M. Cren, N. Nziza, A. Carbasse, P. Mahe, E. Dufourcq-Lopez, M. Delpont, H. Chevassus, M. Khalil, T. Mura, I. Duroux-Richard, F. Apparailly, E. Jeziorski, P. Louis-Plence, *Front. Immunol.* **2020**, *11*, 1716.
- [68] J. Parvizi, B. Zmistowski, E. F. Berbari, T. W. Bauer, B. D. Springer, C. J. Della Valle, K. L. Garvin, M. A. Mont, M. D. Wongworawat, C. G. Zalavras, *Clin. Orthop. Relat. Res.* **2011**, *469*, 2992.
- [69] N. A. Hodges, E. M. Sussman, J. P. Stegmann, *Biomaterials* **2021**, *278*, 121127.
- [70] S. B. Goodman, E. Gibon, J. Pajarinen, T. H. Lin, M. Keeney, P. G. Ren, C. Nich, Z. Yao, K. Egashira, F. Yang, Y. T. Konttinen, *J. R. Soc. Interface* **2014**, *11*, 20130962.
- [71] J. P. Nolan, D. Condello, E. Duggan, M. Naivar, D. Novo, *Cytometry, Part A* **2013**, *83 A*, 253.
- [72] W. G. Telford, D. M. Shcherbakova, D. Buschke, T. S. Hawley, V. V. Verkhusha, *PLoS One* **2015**, *10*, e0122342.
- [73] CeramTec GmbH, *Proven Technology from CeramTec: BIOLOX®delta – Know-How in Large Scale Production – Ceramic Applications*, CeramTec GmbH, Germany **2017**.